#### **REVIEWS**



# A Review of Benchmark Experiments for the Validation of Peridynamics Models

Patrick Diehl<sup>1</sup> • Serge Prudhomme<sup>2</sup> · Martin Lévesque<sup>1</sup>

Received: 2 November 2018 / Accepted: 25 December 2018 / Published online: 12 February 2019 © Springer Nature Switzerland AG 2019

#### **Abstract**

Peridynamics (PD), a non-local generalization of classical continuum mechanics (CCM) allowing for discontinuous displacement fields, provides an attractive framework for the modeling and simulation of fracture mechanics applications. However, PD introduces new model parameters, such as the so-called horizon parameter. The length scale of the horizon is a priori unknown and need to be identified. Moreover, the treatment of the boundary conditions is also problematic due to the non-local nature of PD models. It has thus become crucial to calibrate the new PD parameters and assess the model adequacy based on experimental observations. The objective of the present paper is to review and catalog available experimental setups that have been used to date for the calibration and validation of peridynamics. We have identified and analyzed a total of 39 publications that compare PD-based simulation results with experimental data. In particular, we have systematically reported, whenever possible, either the relative error or the *R*-squared coefficient. The best correlations were obtained in the case of experiments involving aluminum and steel materials. Experiments based on imaging techniques were also considered. However, images provide large amounts of information and their comparison with simulations is in that case far from trivial. A total of six publications have been identified and summarized that introduce numerical techniques for extracting additional attributes from peridynamics simulations in order to facilitate the comparison against image-based data.

**Keywords** Peridynamics  $\cdot$  Benchmark problems  $\cdot$  Validation  $\cdot$  Experimental data  $\cdot$  Fracture mechanics  $\cdot$  Wave propagation  $\cdot$  Visualization techniques

#### 1 Introduction

Peridynamics [113] provides a novel framework for the modeling and simulation of fracture mechanics applications. Peridynamics (PD) can be viewed as a non-local generalization of classical continuum mechanics (CCM), in which the mechanical behavior is modeled in terms of an integral equation of the displacement field rather than by a partial differential equation. The general framework for peridynamics can be further classified into two approaches: (1) bond-based PD [113, 117] and (2) state-based PD [118].

Patrick Diehl patrick.diehl@polymtl.ca

- Department of Mechanical Engineering, Ecole Polytechnique Montréal, Montreal, Canada
- Department of Mathematical and Industrial Engineering, Ecole Polytechnique Montréal, Montreal, Canada

In all cases, the PD formulation allows for discontinuous displacement fields, which may be seen as an attractive feature of the method for the treatment of problems dealing with fracture mechanics. Another advantage of PD is that failure phenomena, like in molecular dynamics or atomistic lattice models, can be explicitly included in the constitutive models. In other words, no other external criterion is needed within the peridynamics framework for modeling the initiation and growth of cracks, in contrast to continuum models. This implies that PD is well suited for the simulation of fracture mechanics applications initially devoid of cracks. We refer to [10, 87] for a general description of PD and to [116] for a review of its advantages.

Although the PD framework appears to be a promising approach for many problems in solid mechanics, a collective effort remains to be done to validate the bond-based and state-based constitutive models in order to gain confidence in the approach's predictability and reliability. In particular, PD introduces new parameters, such as the so-called horizon, that are a priori unknown and need to



be identified. Both calibration and validation processes require experimental data to assess model's adequacy and predictability [41, 42]. Another challenge is the treatment of boundary conditions in the case of non-local models. For example, boundary traction does not naturally appear in the non-local formulation [88], which implies that external loads should be applied in a manner different from that in classical continuum mechanics.

The main objective of this survey paper is to review and catalog the available experimental data that have already been used in the literature for the validation of peridynamics models and simulations. Our goals are essentially to overview the experimental setups and observables that have been achieved so far and to summarize the validation results presented by the authors, if available.

The experiments are classified here into three main categories: (1) the first category is concerned with dynamical experiments that involve wave propagation phenomena; (2) the second category lists the experiments that focus on characterizing the initiation and growth of cracks for various materials; (3) the last category gathers the experiments whose outputs are digital images of observed phenomena. This classification was arbitrarily chosen to simplify the presentation of the experiments.

The experimental data has been classified by type: (1) scalar values of observables; (2) scalar functions of input parameters; (3) and digital images. We report the relative error between experiments and predictions for scalar observables. We estimate the so-called coefficient of determination R-squared [26], also referred to as the Pearson correlation coefficient R, between the data and model predictions for scalar functions, like series of points. Data stored in the form of images provide a large amount of information, which makes comparison with simulations less trivial. It may be necessary to develop advanced visualization methods [60, 61, 140] to take full advantage of the richness of imaging techniques and be able to fully compare the results from non-local model simulations such as those obtained from peridynamics or molecular dynamics. We think that these methods could be useful to the community and therefore report on existing methods, e.g., extraction of fragments or crack surfaces.

We hope that this survey will provide a useful resource for those interested in the validation of PD models. We also believe that such a contribution could lead to the definition of benchmark problems and experiments for the analysis of PD simulations. This has been in fact the source of motivation for writing such a paper.

The paper is structured as follows: Section 2 presents some preliminaries, in particular, the approach that we followed to collect the publications relevant to the survey and a brief description of the method to estimate the coefficient of determination *R*-squared. Section 3 presents the

list of dynamical experiments based on wave propagation phenomena for the validation of crack propagation and Section 4 reviews the experiments used for the validation of crack initiation/propagation. Section 5 reports in a concise fashion the relative error or the coefficient of determination for each of the previous experiments that provide a confidence level in the validity of the peridynamics models. Section 6 describes advanced visualization techniques and methods to extract additional attributes for comparison against experimental data. Section 7 provides conclusions and perspectives on the state-of-the-art in the validation of peridynamics models.

#### 2 Preliminaries

#### 2.1 Literature Search Strategy

Our objectives in this paper were to find published articles dealing with the validation of peridynamics models based on experimental data, either in the form of observational data or digital images. References for this survey were thus collected using the two databases Google Scholar and Web of Science<sup>TM</sup> based on the following search strategy:

- 1. A search with keywords "peridynamics + experiment" and "peridynamics + benchmark" resulted in a total of 53 references, of which 39 papers directly dealt with comparison of simulation results against experimental data. Note that we chose to include a search based on the keyword "benchmark" to find works in which authors used experimental data to verify the implementation of their codes. These papers do not necessarily address model validation. Although we will concentrate on the results of the 39 papers most relevant to this study, the remaining 14 articles are also included in the list of references.
- A search with keywords "peridynamics + computer graphics" and "peridynamics + visualization" was also carried out and resulted in five papers, among which three utilize techniques from computer graphics for the comparison with experimental data and two use peridynamics for physics-based rendering.

#### 2.2 Choice of Validation Metric

Validation processes involve the comparison of metrics and threshold values between experimental data sets and predictions. Many metrics, either statistical or deterministic, have been introduced in the past depending on the nature and availability of data. For consistency throughout the paper, we have chosen to consider two simple metrics.



Table 1

Material	Mechanical test	В	S	Exp	Sim
Plastic polymer (allyl diglycol carbonate or CR-39)	Stress wave propagation (half-plane)	✓		[25]	[93]
ALON/PMMA	Wave speed (edge-on impact experiment)	$\checkmark$		[121–123]	[28, 34, 141]
Aluminum	Split-Hopkinson pressure bar	$\checkmark$		[14, 23]	[64]
Steel (4340 RC 43)	Split-Hopkinson pressure bar		$\checkmark$	[46]	[44]
Sandstone (Bera and Massilion)	Wave dispersion and propagation		$\checkmark$	[133, 143]	[18]

Let us define the relative error between an observable y and the predicted value  $\hat{y}$  as,

$$e_r = \frac{|y - \hat{y}|}{|y|}.\tag{1}$$

Let us consider a series of observables  $y_i$ , i = 1, ..., n, each associated with predicted values  $\hat{y}_i$  that can be computed in terms of a model  $f(x_i)$ , where  $x_i$  denotes the predictor variables. The coefficient of determination  $R^2$  is defined as:

$$R^2 = 1 - \frac{\text{SSE}}{\text{SST}} \tag{2}$$

where the error sum of squares, SSE, and the total sum of square deviations from the average  $\bar{y}$ , SST, are given by:

$$SSE = \sum_{i=1}^{N} (y_i - \hat{y}_i)^2$$
 (3a)

$$SST = \sum_{i=1}^{N} (y_i - \bar{y})^2$$
 (3b)

with

$$\bar{y} = \frac{1}{N} \sum_{i=1}^{N} y_i. \tag{3c}$$

 $R^2$  is a statistical measure ranging from 0 to 1 that indicates how the predictions  $\hat{y}_i$  approximate the data points  $y_i$ . In particular, if  $R^2 = 1$ , i.e. SSE = 0, then the data points and predictions fit perfectly. On the other hand, if  $R^2 = 0$ , i.e., SSE = SST, then all predictions lie on a perfectly horizontal line. In other words, the value of  $R^2$  provides a measure of the correlation between the data points  $y_i$  and the predictions  $\hat{y}_i$ .

Some of the references did not provide any R-square coefficient. In that case, we chose to extract the values from the experimental and simulation data by using the web-based application  $WebPlotDigitizer^1$  and computed the  $R^2$  coefficient using the SciPy package. Note that the computed  $R^2$  value depends on the extraction procedure used to obtain the data from the published figures. The procedure that we followed here was first to take a screen shot of the figures and upload them to the WebPlotDigitizer.

<sup>&</sup>lt;sup>2</sup>https://www.scipy.org/



Then, we selected a range on the curve with tick marks on the x-axis and the y-axis, and provided the corresponding values on the axes. Following this calibration process, we defined uniformly distributed points along the two curves obtained from the experiment and simulation. We acknowledge that the choice of the calibration points and the equidistant points may influence the  $R^2$  value. For a given data set, we repeated the extraction process three times and observed that the variations would be on the order of 2%. We deemed this difference as acceptable.

We wish to emphasize at this point that accessing raw published experimental data in experimental fracture mechanics is difficult. A study of the long-term availability of raw experimental data was carried out in [35]. The main result of the study was that out of the 187 articles published from 2000 to 2016, only 11 data sets were still available and 42% of the authors who were contacted did actually reply. This situation explains why we had to resort to alternatives means to analyze the published data.

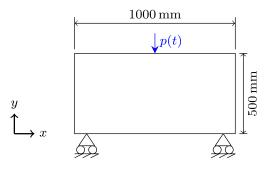
#### **3 Wave Propagation Experiments**

Table 1 summarizes the experiments involving wave propagation phenomena found in the collected publications. The experiments are grouped by bond-based peridynamics (**B**) and state-based peridynamics (**S**) to denote the type of PD formulation that attempted to reproduce the experiment. The type of material used in the experiment and the references for the simulations and experiments are listed as well. The missing  $R^2$  coefficient and relative errors were also evaluated when applicable. Most of the figures in this section, have been adapted and extended from those in the corresponding articles. To distinguish between the measurements and the applied load, the applied load was colored in blue.

#### 3.1 Propagation of Stress Waves in a Half-Plane

Nishawala et al. [93] studied the propagation of stress waves in an allyl diglycol carbonate (CR-39) half-plane. The sample's length, the height, and the thickness were 1000 mm, 500 mm, and 6.655 mm, respectively (Fig. 1).

<sup>&</sup>lt;sup>1</sup>https://automeris.io/WebPlotDigitizer/



**Fig. 1** Geometry of the half-plane [25] where a triangular pulse load p(t) of 20  $\mu$ s with maximum amplitude 20.7  $\times$  10<sup>3</sup> N was applied to the top and at the middle of the plate thickness 6.655 mm. The plate's material was allyl diglycol carbonate or CR-39

An triangular impulse load of  $20\,\mu s$  with maximum amplitude of  $20.7 \times 10^3$  N was applied to the top edge using a semi-cylindrical pit. Nishawala et al. [93] compared experimentally measured displacements [25] in *x*-direction (m) as a function of the position (m), for three different times. The final simulation time was  $208\,\mu s$ . The  $R^2$  correlation is 0.74 at  $60\,\mu s$ , 0.35 at  $92\,\mu s$ , and 0.15 at  $139\,\mu s$ . Nishawala et al. [93] concluded that additional studies for the relation between the horizon and wave speed were needed.

#### 3.2 Edge-on Impact Experiment

The edge-on impact (EOI) experiment is designed to visualize dynamic fracture in brittle materials using a high-speed photographic technique [122]. In this experiment, a cylinder hits a square plate on one edge, at a high velocity. Figure 2 shows the dimensions of the experimental setup. The wave front velocity and the impact damage visualization for aluminum oxynitride (ALON) and polymethyl methacrylate (PMMA) [90, 121–123] were addressed in Diehl et al. [34] and Zhang [141].

Fig. 2 Sketch of the geometry of the edge-on impact (EOI) experiment: a front view and b side view. A cylindrical striker hits the back of the plate at a high velocity. A high-speed photographic technique is utilized for visualizing the dynamic fracture in brittle materials

Zhang [141] compared the simulated and experimentally measured average propagation speed of the primary damage front [90]. The average propagation speed in the simulation was estimated at about 8.7 km s<sup>-1</sup> while the corresponding value measured in experiments was about 8.4 km s<sup>-1</sup>. The propagation speed of individual cracks obtained from PD simulations was about 4.8 km s<sup>-1</sup> and about 4.6 km s<sup>-1</sup> for cracks growing in *y*-direction. In comparison, the value obtained from experiments was about 4.4 km s<sup>-1</sup>.

Diehl et al. [34] compared the predicted wave speed of the damage front with that measured in [121–123] and reported a relative error  $e_r$  of 10%. Diehl et al. [34] studied various convergence scenarios considered in [38], as shown in Fig. 3. In this work, the best results with respect to the relative error were obtained using a horizon of three times the nodal spacing, as suggested in [115]. The horizon in [115] was adjusted such that the peridynamics simulations produce the same dispersion curves (frequency (Hz) vs phase velocity of the longitudinal waves (m s<sup>-1</sup>)) as those measured in experiments for a given material.

#### 3.3 Split-Hopkinson Pressure Bar

PD simulations of wave propagation phenomena in a Split-Hopkinson pressure bar (SHPB) [14, 23] were performed by Jia [64] in the case of steel. SHPB is usually used for determining the dynamic stress-strain response of metals [57, 76]. Figure 4 shows a diagram of the SHPB experimental setup, which consists of three bars: the striker bar, the incident bar, and a transmission bar. The specimen is placed between the incident bar and the transmission bar. The striker bar impacted the incident bar at a velocity of 17.5 ms<sup>-1</sup> and a wave propagated through the bars. The black dots represent strain gages used to measure the strain variations produced by traveling waves. Jia [64] compared the predicted strain as a function of time with experimental results up to 2 ms. Using the experimental data provided in [23], the  $R^2$  coefficient is evaluated at 0.99, which is a very good fit to the experimental time series.

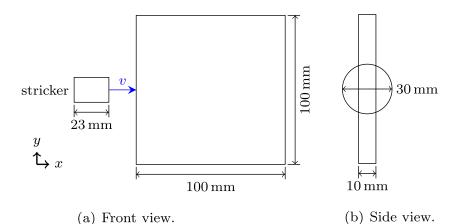
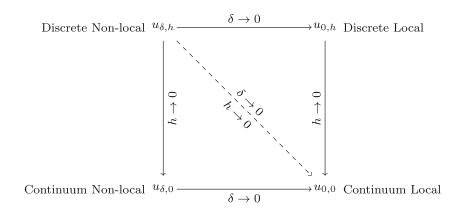




**Fig. 3** Different convergence scenarios for the nodal spacing h and the horizon  $\delta$  [38]



Foster et al. [44] also studied the Hopkinson pressure bar experiment [46]. Figure 4 depicts the sketch of the experimental setup. Their objective was to compare the predicted true strain - stress curves with the experimentally measured curves, for various strain rates. The  $R^2$  coefficient was computed here as 1.00 and 0.97 in the cases of strain rates of  $1150 \, \mathrm{s}^{-1}$  and  $2900 \, \mathrm{s}^{-1}$ , respectively.

### 3.4 Wave Dispersion in Bera and Massilion (Dry) Sandstone

Wave dispersion (frequency (Hz) vs phase velocity of the longitudinal waves (m s<sup>-1</sup>)) and propagation in two different types of sandstone (Berea and Massilion) [133, 143] was studied by Butt et al. [18] for different levels of confining pressures (10, 20, and 40 MPa). Figure 5 shows the geometry of the square plate (1500 mm  $\times$  1500 mm) with a thickness of 2 mm. A time-dependent load in displacement propagating in *y*-direction is applied to the center (x = y = 750 mm) of the square plate.

Butt et al. [18] compared the predicted and experimental dispersion curves. For both sand stones, the experimental dispersion data measured at a confining pressure of 20 MPa [133] was used to fit the peridynamic model parameters. The  $R^2$  coefficient between the fitted material parameters and the experimental data used for the fitting was estimated

at 1.00 and 0.93 for the Massilion sandstone and Berea sandstone, respectively.

The calibrated model was subsequently used to validate the predictions made for confining pressures of 10 MPa and 40 MPa. Table 2 shows the  $R^2$  correlation for the experimental data obtained for different confining pressures. Butt et al. [18] reported excellent agreement when the calibrated material properties for 20 MPa were used at various confining pressures.

# 4 Crack Initiation and Propagation Experiments

Table 3 lists the mechanical tests found in the literature that dealt with crack initiation and propagation for the validation of peridynamics models. We grouped the publications with respect to the type of materials involved, namely, composite, steel/aluminum, glass, concrete, and other materials. Table 3 also lists the type of experiments, the PD models used in the simulations, where  $\bf B$  refers again to bond-based peridynamics and  $\bf S$  to state-based peridynamics, and the corresponding references. The missing values of the  $R^2$  coefficient and relative error where also evaluated, when applicable.

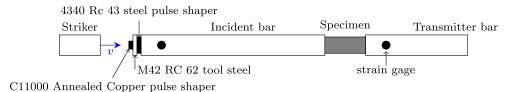
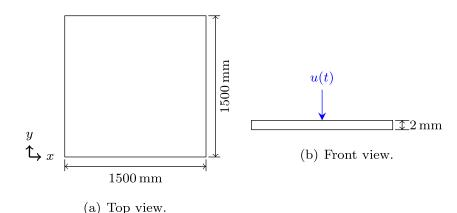


Fig. 4 Sketch of the experimental setup of the Split-Hopkinson pressure bar (SHPB), also referred to as the Kolsky's bar. The SHPB experimental setup which consists of three bars: the striker bar, the incident bar, and a transmission bar. The striker bar impacts the

incident bar at a velocity of 17.5 ms<sup>-1</sup>, which induces a wave that propagates through the bars. The black dots represent strain gages used to measure the strain variations produced by traveling waves. In [46] the SHPB bar was extended by a pulse shaper



**Fig. 5** Sketch of the geometry: **a** top view and **b** front view. A time-dependent load in displacement propagating in *y*-direction is applied to the center (x = y = 750 mm) of the square plate



#### 4.1 Composites

#### 1. Dynamic crack growth around stiff inclusion

The dynamic growth of a crack around a stiff inclusion was numerically studied with peridynamics by Agwai et al. [2]. In [75], an 140 mm  $\times$  42 mm  $\times$  8 mm epoxy, embedded with a central stiff glass inclusion (fiber) of diameter d = 4 mm and featuring an initial crack, is impacted at a velocity of 5.3 m s<sup>-1</sup> using a pneumatic hammer with a hemispherical tip. Figure 6 depicts the setup. Experiments were conducted for specimens with weakly and strongly bonded fibers. Agwai et al. [2] qualitatively compared the predicted crack paths for weak and strong interfaces in the visualized simulation results with those observed in the images during the experiments. The objective of the study was primarily to investigate the influence of the bonding interface on the crack path. The simulations qualitatively captured the different failure modes that were observed in the experiment.

**Table 2** Butt et al. [18] used the experimental data [133] to calibrate the peridynamics material parameters at a confining pressure of 20 MPa

Sandstone $R^2$		Confining pressure (MPa)
Fitting		
Massilion	1.00	20
Berea	0.93	20
Validation		
Massilion	0.97	10
Berea	0.84	10
Massilion	0.96	40
Berea	0.95	40

These calibrated material parameters were used for the comparison against experiments at confining pressure of 10 MPa and of 40 MPa

### 2. Damage growth in a double-lap joint test using a six-bolt specimen

Oterkus et al. [96] simulated the initiation and propagation of damage in a six-bolt carbon fiber/epoxy system (HTA7/6376) specimen [120] during a fatigue experiment. The fatigue behavior of a double-lap bolted joint with multiple fasteners was induced by subjecting the specimen to a cyclic tensile load  $\sigma_{\min}/\sigma_{\max} = -1$  until failure. Figure 7 depicts the sample's geometry.

Oterkus et al. [96] quantitatively compared the simulated and predicted failure modes using photo micro graphs. Failure essentially occurred in the matrix near the bolt holes. The failure modes predicted in the simulations were consistent with the experimental observations in the images.

#### 3. Progressive damage in center-cracked laminates

Kilic et al. [70] simulated the crack initiation and growth in center-cracked laminates using peridynamics and compared their results with the experimental observations in [6, 69, 134]. Figure 8 shows the rectangular plate utilized in the simulations of dimension 10.16 mm×5.08 mm having an initial crack of length 1.27 mm. The plate is made of four plies of thickness 0.0413 mm each so that its total thickness is 0.1651 mm. The uniform tension applied in experiment [134] is gradually applied by prescribing the velocity boundary conditions  $v = \pm 1.27 \times 10^{-7}$  mm per time step at the nodes located within a distance of 0.097 mm from both vertical ends. Note that they used a 15 times smaller inplane dimension than the one in the experiment [106], due to limitation in the computational resources. For lamina the elastic properties of T800/3900-2 pre-preg tape reported by [106] were chosen. Lamina orientations of fibers are 0° fibers are running parallel to the x-axis and 90° fibers are running parallel to the y-axis. The stacking sequences  $[0^{\circ}/90^{\circ}/0^{\circ}]$  and  $[0^{\circ}/45^{\circ}/0^{\circ}]$ were considered for three-ply laminates. Kilic et al. [70] obtained an asymmetric delamination pattern due to the presence of a 45° ply.

Moreover, the multiple splitting around the crack tip was also observed in [6]. Finally, Kilic et al. [70]



Table 3 Applications of bond-based and state-based peridynamics for the comparison with experimental data

Material	Mechanical test	В	S	Exp	Sim
Composite	Flexural test with an intial crack	<b>√</b>		[75]	[2]
Composite	Damage growth prediction (six-bolt specimen)	$\checkmark$		[120]	[96]
Composite	Damage prediction (center-cracked laminates)	$\checkmark$		[6, 12, 69, 134]	[70]
Composite	Dynamic tension test (prenoteched rectangular plate)	$\checkmark$		[12, 65]	[58]
Steel	Crack growth (Kalthoff-Winkler)	$\checkmark$	$\checkmark$	[66–68]	[3, 52, 114, 144]
Aluminum/Steel	Fracture (compact tension test)	$\checkmark$		[9, 77, 89, 91]	[135, 141, 142]
Aluminum	Taylor impact test		$\checkmark$	[4, 21]	[3, 43, 45]
Aluminum (6061-T6)	Ballistic impact test		$\checkmark$	[132]	[127]
Concrete	Lap-splice experiment	$\checkmark$		[48]	[48]
Concrete	3-point bending beam	$\checkmark$	$\checkmark$	[19, 63]	[7, 51]
Concrete	Failure in a Barazilian disk under compression		$\checkmark$	[51]	[54]
Concrete	Anchor Bolt Pullout	$\checkmark$		[128]	[83]
Glass	Dynamic crack propagation (prenotched thin rectangular plate)	$\checkmark$		[15, 36, 100]	[2, 53, 144]
Glass	Impact damage with a thin polycarbonate backing	$\checkmark$		[8, 20, 40]	[59]
Glass	Single crack paths (quenched glass plate)	$\checkmark$		[13, 103, 136]	[71]
Glass	Multiple crack paths (quenched glass plate)	$\checkmark$		[102, 137]	[71]
Glass	Crack tip propagation speed	$\checkmark$		[15]	[52, 53, 144]
PMMA	Fast cracks in PMMA	$\checkmark$		[39]	[2]
PMMA	Tensile test	$\checkmark$		[124]	[32]
Soda-lime glass	Impact on a two-plate system	$\checkmark$		[16, 130]	[130]

Legend: B refers to bond-based peridynamics, S refers to state-based peridynamics, Exp to experimental data, and Sim to simulation

predicted that the crack propagated along the direction parallel to the fibers within the plies oriented at 45° and 90°. This behavior was also detected in [134].

# 4. Dynamic tensile test on a pre-notched rectangular plate

A dynamic tensile test performed on a prenotched rectangular 0° UD composite plate (M55J/M18 carbon/epoxy) [12, 65] was considered in Hu et al. [58]. Figure 9 shows a diagram of the 200 mm×100 mm plate with an initial crack of length 25 mm subjected

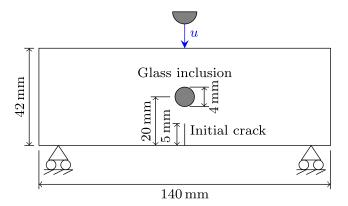


**Fig. 6** Sketch of the geometry with a width of 8 mm used in [75]. A pneumatic hammer with a hemispherical tip is used to induce an impact at a velocity of  $5.2 \,\mathrm{m\cdot s^{-1}}$  in the center of the top of the plate

to a uniform tensile load  $\sigma$  of  $\pm 40$  Pa. The simulations showed a symmetric path of splitting fracture mode and bond breaking only in the matrix, which is consistent with the experiments [12].

#### 4.2 Steel and Aluminum Materials

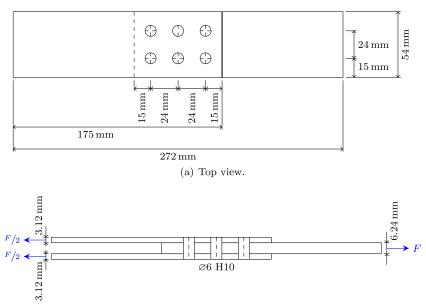
#### 1. Kalthoff-Winkler experiment

The Kalthoff-Winkler experiment consists in striking a plate featuring two initial cracks of length 50 mm in the middle with a steel impactor, as sketched in Fig. 10. The observable in this experiment is the crack angle, along with the fact that the cracks propagate through the free surface [66–68]. The crack propagates from the initial crack tip at an angle around 68° with respect to the initial crack direction.

Silling [114] correctly predicted the crack angle with respect to that measured in the experiment and observed that the cracks propagated all the way to the free surface. Amani et al. [3] and Zhou et al. [144] reported that the crack angle predicted by the state-based PD model matched the angle observed in the experiments. Gu et al. [52] also showed that the crack angle and final crack path were qualitatively in good agreement with the experimental observations, even if the crack initiation time obtained in the simulations, 28 µs, was



Fig. 7 Sketch of the geometry (top view (a) and front view (b)) of six-bolt composite specimen [120]. The specimen plates were joined by six titanium bolts with protruding hexagon heads



(b) Front view.

slightly lower than that measured in the experiments, 29 µs.

#### 2. Compact tension experiments

Compact tension (CT) tests are used to study fracture in metals [89, 91, 131] and are standardized by ASTM E647-00 [5] and ISO 7539-6 [62]. Figure 11a shows a plate specimen of dimension 126 mm×121 mm with four circular cutouts. For this configuration, Yolum et al. [135] simulated the crack mouth opening (in mm) with respect to the applied force (in kN) and compared their results with the experimental results of [77, 89]. For aluminum alloy (D16AT) CT specimens with four and eight circular cutoffs, the  $R^2$  coefficient was computed as 1.00 in both cases. For a plate devoid of cutoff, the  $R^2$  coefficient, using the experimental results provided in [131], is 1.00. Zhang [141, 142] simulated the crack paths observed in [91] on a modified CT test [142], whose configuration is shown in Fig. 11b. The dimensions of the plate are in this case

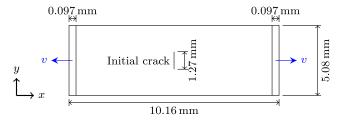


**Fig. 8** Sketch of the center-cracked laminate used by Kilic et al. [70] which is smaller than in the experiments due to computational limitations. The uniform tension applied in experiment [134] is gradually applied by prescribing the velocity boundary conditions  $v = \pm 1.27 \times 10^{-7}$  mm per time step at the nodes located within a distance of 0.097 mm from both vertical ends

40 mm×40 mm×8 mm. Subsequently, Zhang [141] simulated the position (X, Y) (in mm) of the crack path and the fatigue life for three values of the PD horizon, i.e.,  $\delta = \{0.6, 1.2, 2.4\}$  mm. In the case of the modified CT test, the  $R^2$  coefficient for the crack path positions and fatigue life is given by  $R^2 = 0.99$  and  $R^2 = 0.99$  for  $\delta = 0.6$ , and  $R^2 = 0.97$  and  $R^2 = 0.99$  for  $\delta = 1.2$ , respectively. Zhang reported that the case  $\delta = 2.4$  produces a short line in the plots due to a different crack path. Therefore, this case is not considered for the  $R^2$  correlation.

#### 3. Taylor impact experiments

A Taylor impact test [4, 21], in which a cylindrical projectile is shot on a hard target, was considered by Amani et al. [3] and by Foster et al. [43, 45]. The experiment is designed for low velocity impacts in order to induce relatively small deformations. Amani et al. [3] qualitatively compared the post test deformation using dynamic structural light (DSL) images from [4] with the deformation obtained from their simulations. Moreover, Foster et al. [45] compared the normalized length and diameter of the damage as a function of the impact velocity for the same experiment.

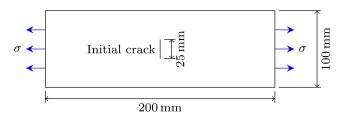


Fig. 9 Sketch of the pre-notched rectangular 0° UD composite plate in the dynamic tensile test with  $\sigma \pm 40$  Pa [12, 65]



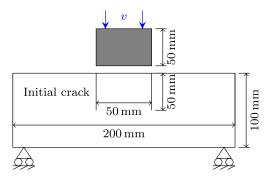


Fig. 10 Sketch of the geometry considered in the Kalthoff-Winkler experiment [66-68] where a spherical impactor strikes the plate with a velocity  $32\,\mathrm{ms}^{-1}$ 

The coefficient of determination was estimated as  $R^2 = 1.00$  and  $R^2 = 0.99$  for the normalized length and normalized diameter, respectively. The true stress, as a function of the Lagrangian strain, was also estimated and compared to the experimental results of [21]. The  $R^2$  coefficient is in this case equal to 0.96.

#### 4. Ballistic impact test

A ballistic impact test was simulated by Tupek et al. [127] using state-based peridynamics and compared to the experimental results of [132], in which a hard-steel spherical projectile of diameter 13.97 mm, impacted an extruded 6061-T6 aluminum sandwich panel (Fig. 12) with a velocity of 370 m s<sup>-1</sup>, 530 m s<sup>-1</sup>, or 900 m s<sup>-1</sup>. The observable in the experiment was the residual velocity versus the impact velocity. The predicted values of the observable lead to a  $R^2$  coefficient of 0.99.

#### 4.3 Glassy Materials

#### 1. Crack paths in a quenched glass plate

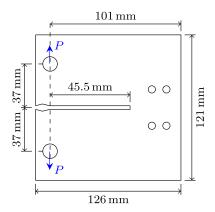
Experiments with single crack path [13, 103, 136] and multiple crack paths [102, 137] in a quenched

glass plate were numerically studied by Kilic et al. [71]. In the experimental setup, a thermal stress was applied to the plate by placing it between two heat reservoirs. Depending on the specimen size and temperature difference, three types of crack propagation path were observed in the experiments: straight crack, oscillating crack, and branched crack as shown in Fig. 13. The rectangular thin plate of dimension 24 mm×64 mm×0.4 mm featuring a single initial crack, similar to the one used in the experiment [136], is shown in Fig. 14a. Kilic et al. [71] predicted straight cracks for small temperature differences and observed that the crack would oscillate first and then propagate in a straight direction for intermediate temperatures, and that crack branching would occur at higher temperatures. In other words, the PD simulations were able to capture most of the observed crack behaviors with respect to the temperature differences. Figure 14b shows the plate of dimension 48 mm×64 mm×0.4 mm for the setup with multiple cracks. Kilic et al. [71] numerically studied a plate with 2, 3, 5, 6, 7, 10, and 16 initial cracks and observed that there is an upper limit on the number of cracks that can propagate inside a specific plate. This is consistent with the experimental results in [102].

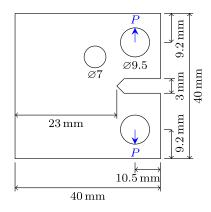
## 2. Crack propagation speed in a pre-cracked glass plate

Gu et al. [52] used the bond-based PD model to study the propagation speed of a crack in a pre-cracked glass plate subjected to a step tensile loading. Gu et al. [52] considered the plate of dimension 100 mm×40 mm with an initial crack of length 50 mm, as shown in Fig. 15. Gu et al. [52] computed the crack propagation speed (in ms<sup>-1</sup>) as a function of time ( $\mu$ s) and compared it against the maximal fracture velocity  $v_F = 1580 \text{ m s}^{-1}$  obtained in the experiment in [15]. The maximal propagation speeds obtained in the simulations were as

Fig. 11 Sketches of the compact tension (CT) tests used to study fracture in metals [89, 91, 131] and standardized by ASTM E647-00 [5] and ISO 7539-6 [62]. a CT tension test with four holes and b modified geometry



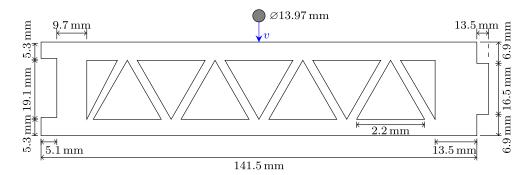
(a) Compact tension test with four circular cutouts of 4 mm [89].



(b) Modified geometry of the compact tension test used in [91].



Fig. 12 Cross section of the extruded corrugated 6061-T6 aluminum structure utilized in the ballistic impact test [132]. A spherical impactor of 13.97 mm strikes the structure for different values of the velocity  $\nu$ :  $370 \, \mathrm{m \ s^{-1}}$ ,  $530 \, \mathrm{m \ s^{-1}}$ , and  $900 \, \mathrm{m \ s^{-1}}$ 



follows: 2037 m s<sup>-1</sup> for a uniform mesh with 16281 discrete PD nodes, 2341 m s<sup>-1</sup> for a uniform mesh with 4141 discrete PD nodes, and 2699 m s<sup>-1</sup> for an adaptive mesh with 414 discrete PD nodes up to 7227 discrete PD nodes. Zhou et al. [144] and Ha et al. [53] computed a maximum fracture speed of 1157 m s<sup>-1</sup> and 1679 m s<sup>-1</sup>, which are 1.45% lower and 6% larger than the experimental value, respectively.

#### 3. Crack growth in a pre-notched glass sheet

Crack growth in a pre-notched glass sheet [100] under tensile loading was studied by Agwai et al. [2]. Figure 15 depicts the pre-notched plate of dimension 100 mm×40 mm and the initial crack of length 50 mm. The PD simulations and experiments both put in evidence that the crack splits into two branches, which grow until they eventually reach the right boundary.

### 4. Fast crack growth in an edge-cracked plate under tension

Fast growth of a crack in an edge-cracked PMMA plate under tension [39] was considered by Agwai et al. [2]. The plate had dimension of 380 mm $\times$ 440 mm and the initial crack was 4 mm long, as shown in Fig. 16. The crack velocity predicted over the time period up to 80  $\mu$ s was compared with the velocity obtained in the experiment, ranging from 0 to 1000 m s<sup>-1</sup>. The

corresponding  $R^2$  coefficient was evaluated in this case as  $R^2 = 0.72$ .

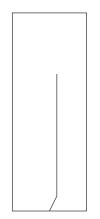
#### 5. Impact damage on a thin glass plate with polycarbonate backing

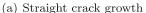
Impact damage on a thin glass plate with poly carbonate backing [8, 20, 40] was studied by Hu et al. [59]. They qualitatively compared the damage patterns in the glass layer under three projectile speeds. Hu et al. [59] reported that the main fracture patterns observed experimentally were correctly captured.

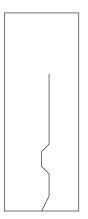
#### 6. Tensile test

A tensile test [124] was simulated by Diehl et al. [32] using a bond-based PD model. The objective was to predict the Poisson ratio of a PMMA sample under a time-dependent loading for different values of the horizon parameter  $m \in \{4, 5, ..., 12, 13\}$ . Thus, the neighborhood  $B_{\delta}(x_i)$  of a discrete PD node  $x_i$  contains 2m+1 nodes in  $[x_i-\delta,x_i+\delta]$  in each direction [11]. The  $R^2$  coefficient of the Poisson ratio as a function of time was obtained as 0.65. Note that the parameters of the exponential model considered in this study depended on the energy release rate and shear modulus, and not on the horizon, as in many other models. The horizon in the model was determined by the failure strain, which can be measured during the tensile test.

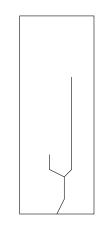
Fig. 13 Schematics of the crack growth depending on the specimen size and temperature difference: straight crack (a), oscillating crack (b), and branched crack (c) observed in experiment [136]







(b) Oscillating crack growth



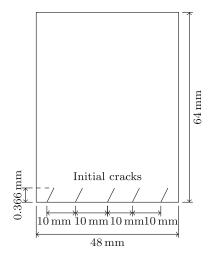
(c) Branched crack growth



Fig. 14 Sketches of the single crack (a) and multiple crack glass plate (b). In the experimental setup, a thermal stress was applied to the plate by placing it between two heat reservoirs to initiate the crack growth



(a) Geometry of the glass plate with single crack similar to the experiment in [136].



(b) Glass plate with 5 initial cracks. The same geometry was used with 2, 3, 6, 7, 10, and 16 initial cracks in [102, 137].

#### 4.4 Concrete

#### 1. Lap-splice experiment

Gerstle et al. [48] presented simulation and laboratory results of a reinforced concrete lap-splice benchmark problem. Gerstle et al. [48] quantitatively compared the crack pattern obtained in the laboratory experiment and in the simulations. The crack pattern observed in the experiment consisted of two or three longitudinal splitting cracks, each one being approximately co-planar with the axis of the concrete cylinder. However, the crack patterns predicted by the PD simulations were quite different and the authors suggested that such a difference could be explained by variations in the loading rates.

#### 2. **3-point bending beam experiment**

Gu et al. [51] performed some simulations of a 3-point bending beam experiment [63]. Figure 17 illustrates the plate (320 mm $\times$ 70 mm) used in the experiment. The velocity applied at the top of the beam

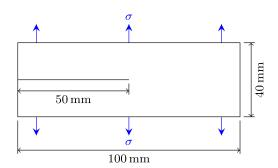


Fig. 15 Sketch of the geometry of pre-cracked glass plate under step tensile loading [15, 100]

was  $v = 0.075 \,\mathrm{mm} \,\mathrm{min}^{-1}$ . The objectives of the study were twofold: (1) to accurately predict the crack pattern observed in the experiment [63], which was actually the case; (2) to predict the crack mouth opening displacement with respect to the load. The experimental and simulation data give in this case a coefficient of determination of  $R^2 = 0.61$ .

# Crack mouth opening displacement and load point displacement

Aziz [7] performed simulations of the crack mouth opening displacement versus the applied load (CMOD-load) for three different configurations (D3, D6, and D9) as shown in Fig. 18 and Table 4 [19]. The values of the  $R^2$  coefficient are collected in Table 5. Here, we observe that the values of  $R^2$  vary depending

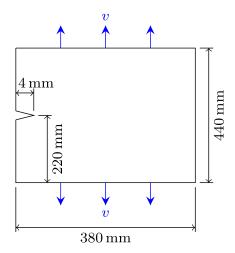


Fig. 16 Sketch of the experimental setup of the dynamic crack growth [39]



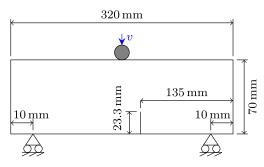


Fig. 17 Sketch of the 3-point bending experiment [19, 63] with an initial crack. The velocity applied at the top of the beam was  $v=0.075\,\mathrm{mm\,min^{-1}}$ 

on the length and position of the notch. The crack mouth opening displacement is usually insensitive to concrete damage at the loaded point and support. Alternatively, the load point displacement, a quantity that is very sensitive to the damage in concrete at the load points, was also computed with respect to the applied load (LPD-load). We observe in Table 5 that the coefficient  $R^2$  suffers a non-negligible drop for D9. In a different exercise, the damage model was calibrated with respect to the experimental CMOD-load diagrams and simulations for the CMOD-load were repeated. The new values of  $R^2$  are also reported in Table 5.

#### 4. Failure in a Brazilian disk

Failure in a Brazilian disk in compression [54] was considered by Gu et al. [51]. Figure 19 shows the diagram of a Brazilian disk of diameter d=100 mm with an initial crack of 30 mm at the center of the disk subjected to a compressive velocity boundary condition  $v=0.05~{\rm m~s^{-1}}$ . The objective of this problem was to reproduce the crack pattern observed in the experiment when the crack propagates through the disk. Gu et al. [51] reported that the numerical results were similar to the experimental ones. They also concluded that non-ordinary state-based PD could be important in the future for the prediction of damage processes.

#### 5. Anchor bolt pullout experiment

The Anchor bolt pullout experiment [128], shown in Fig. 20, was simulated by Lu et al. [83]. In this

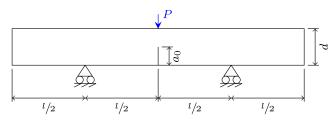


**Fig. 18** Sketch of the 3-point bending with an initial crack for the three configurations D1–D3. The measurements for each configuration are shown in Table 4

**Table 4** The dimensions in mm of the three different configurations of the beam D1–D3 shown in Fig. 18

Depth (d)	Span (l)	Noth depth $(a_0)$
76.2	228.6	25.4
152.4	457.2	59.8
228.6	685.8	76.2
	76.2 152.4	76.2 228.6 152.4 457.2

The width 152.4 mm and the notch width 2.54 mm were the same for all three configurations

experiment, the concrete structure is fixed with two anchors and the bolt is pulled out. Measurements considered for three configurations [128] are shown in Table 6. For these three configurations, the peak loads were predicted and compared to the values obtained in the experiments (see Table 7). For one of these configurations, the load-displacement response (in kN versus  $\mu$ m) was recorded and simulated: the calculation of the corresponding coefficient of determination yielded  $R^2 = 0.92$ . Finally, the failure mode was quantitatively assessed with respect to the experimental observations and the conclusion was that the crack direction and crack branching obtained in the PD simulations were in good agreement with those observed in the experiments.

#### 4.5 Other Materials

#### 1. Rupture phenomena in bio-membranes

The rupture phenomenon in bio-membranes [49] was considered by Taylor et al. [125]. The objective in this experiment was to compare the fractal dimension of ruptures in actual membranes with that extracted from PD simulations. The fractional dimension was post-processed from the computer simulations via image processing techniques and the reticular cell counting (box counting) method. The predicted fractional

**Table 5** Coefficient of determination  $\mathbb{R}^2$  for configurations (D3, D6, and D9) associated with the CMOD-load and LPD-load of a 3-point bending beam

Coefficient of determination $\mathbb{R}^2$				
Configuration	CMOD-load	CMOD-load (Calibrated model)	LPD-load	
D3	0.85	0.37	0.87	
D6	0.89	0.59	0.83	
D9	0.77	0.77	0.51	

In the case of the CMOD-load, the damage model was also calibrated against the experimental CMOD-load data and simulations were repeated



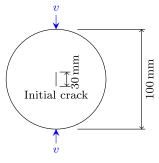


**Fig. 19** Experimental setup of a Brazilian disk in compression [54]. A compression load of  $\pm$  0.05 m s<sup>-1</sup> was applied at the lower and upper tips of the disk

dimensions, namely 1.7, 1.63, and 1.56, computed for different shear moduli, were close to the fractional dimension, 1.7, obtained in the experiment.

#### 2. Crushing of brittle ice against vertical structures

The PD simulation of brittle ice [119] crushed by a vertical structure was performed by Liu et al. [81]. In the experiment, a thin layer of ice of dimension 1000 mm×1000 mm×60 mm is cut in the middle by a rotating cylindrical structure. The mean force and the peak force in the ice obtained in the simulations were compared with those measured in the experiments for several values of the penetration velocity. Table 8 lists these values. We observe that the relative error strongly depends on the velocity of the cylinder.

#### 3. Cross-sectional nanoindentation

Oterkus et al. [95] studied the crack patterns for cross-sectional nanoindentation (CSN) [105]. Figure 21 sketches the rectangular silicon substrate specimen with three layers of copper metallization embedded in inter layer dielectric (ILD) and etch stops (ES) [94]. In the

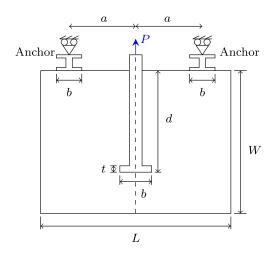


**Fig. 20** Experimental setup of the anchor bolt pullout [128] for the three different configurations shown in Table 6. In this experiment, the concrete structure is fixed by using two anchors and the bolt is pulled out

**Table 6** Measurements for the three different configurations [83] for the sketch shown in Fig. 20

Configuration	W (mm)	L (mm)	a (mm)	d (mm)	b (mm)	t (mm)
1	300	300	100	50	15	5
2	600	600	200	100	30	10
3	900	900	300	150	45	15

experiment, the silicon substrate was indented by a Berkovich diamond, which induced a V-shaped crack. Note that in the simulation, an initial 40° V-shaped crack was introduced similarly as in the experiment. Along the normal to the crack faces, a velocity of  $\pm~0.5~{\rm m~s^{-1}}$  was applied. The crack paths observed in the simulation and experiment showed that the main crack propagated through the silicon and the first layer of copper metallization embedded in interlayer dielectric.

### 4. Dynamic crack propagation in functionally graded materials

Experiments of dynamic crack propagation in functionally graded materials (epoxy/soda-lime glass) (FGM) [1, 73, 74] were used for comparison with PD simulations by Cheng et al [24]. The experimental setup consisted of a plate of dimension 152 mm×43 mm with an initial crack of length 8.6 mm subjected to 3-point loading, as shown in Fig. 22. First, the crack pattern observed in the experiment [74] was quantitatively compared with that obtained in the simulation. The conclusion of this study was that, despite the fact that the dynamic loading used in the simulations was different from that in the experiments, a close resemblance between the predicted and experimental crack paths could still be observed. Second, the evolution of the crack length over time [73] was considered for two cases: (1) pre-crack on the stiffer side  $(E_1 > E_2)$  and (2) pre-crack on the more compliant side  $(E_1 < E_2)$ . When using the linear curve fit of elastic modulus and density to compute the peridynamics micro modulus, the  $R^2$  coefficient is 0.99 for  $E_1$  <  $E_2$  and 0.99 for  $E_1$  <  $E_2$ . When using the piece-wise linear variation measured from the experiments, the  $R^2$  coefficient is now given by 0.98 for  $E_1 < E_2$  and 0.99 for  $E_1 < E_2$ .

**Table 7** Relative error in the predicted peak loads [83] with respect to those obtained in the experiments [128]

Configuration	Simulation (kN)	Experiment (kN)	Relative error (%)
1	17.04	13.4	27.2
2	28.86	14.5	17.8
3	37.48	33.6	11.6



**Table 8** Mean forces and peak forces in ice obtained from experiments and PD simulations. Table is adapted from [81] and completed with values of the relative error

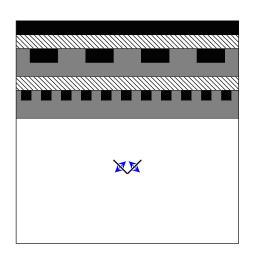
	Mean fo	orce (kN)		Peak fo	rce (kN)	
$v(\text{mm s}^{-1})$	Sim	Exp	$\epsilon_{\mathrm{rel}}$ (%)	Sim	Exp	$\epsilon_{\mathrm{rel}}$ (%)
50	13848	5.3859	74.29	44379	130527	66.00
130	13739	17309	20.63	46342	52479	11.69
210	14324	19136	25.15	49742	38522	29.13

# 5 Summary of Validation Results for Peridynamics Modeling

We reported the  $R^2$  values with respect to the Young's modulus of the materials to create a visual representation of the results. We emphasize that the relative error and coefficient of determination are two measures among many others to quantify the fitness of the simulations to the experimental data. The reasons to choose these measures are twofold: first, they are commonly used in the field and, second, it was relatively straightforward to compute them from the available data since most of the values were missing in the publications. Needless to say that other choices of measures could yield different conclusions. Tables 9 and 10 list the relative error and the  $R^2$  coefficient between the experimental data and the values predicted by the PD simulations, respectively. Likewise, Figs. 23 and 24 provide the same information, but shown with respect to the Young modulus of the material.

Figure 23 suggests that the relative error is consistently smaller than 20% for aluminum and steel, which shows that simulations can predict well the experimental results. For concrete materials, the relative error ranges between 10 and 30%. For glassy materials, it is between 3 and 71%. In the case of crushing-brittle ice by a rotating cylinder, the relative error lies in the range between 14 and 74% for three different rotating velocities.

Fig. 21 Sketch of the rectangular silicon substrate specimen with three layers of copper metallization embedded in interlayer dielectric (ILD) and etch stops (ES). In the experiment [94], the silicon substrate was indented by an Berkovich diamond, which induced a V-shaped crack [105]. Note that in the simulation an initial 40° V-shaped crack was introduced similarly as in the experiment. On the normal to the crack faces a velocity of  $\pm 0.5 \text{ m s}^{-1} \text{ was applied}$ 



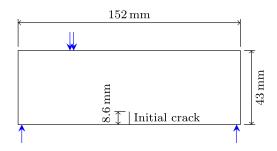


Fig. 22 Sketch of the 3-point loading experiment with boundary conditions

Conclusions in the case of series of observables, based on Fig. 24, are as follows. For aluminum and steel, the coefficient  $R^2$  is in general greater than 0.9, which indicates a very good agreement between simulations and experiments. For concrete materials,  $R^2$  ranges between 0.5 and 0.9 while for glassy materials, it is between 0.6 and 0.72. In the case of functionally graded materials (FGM) and for sandstone, the coefficient reaches values as high as 0.99 and 0.93, respectively. We thus observe that PD simulations usually agree well with experiments involving metallic materials, such as steel and aluminum, and sandstone.

### 6 Extraction of Additional Attributes from Non-local Simulation Data

In peridynamics, information, such as reconstructed stress or strain, is usually provided at the node level. However, quantities measured in experiments are often given at a larger scale. Here, advanced visualization techniques can be utilized to extract missing information or to post-process the solutions in order to be able to compare predictions and experiments.

We collect in Table 11 some information about applications in which visualization techniques were used to

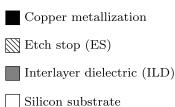




Table 9 Relative error between the observable measured in the experiment and obtained in the simulation

Material	Mechanical test	Observable	Rel. error (%)	Exp	Sim
ALON	Edge-on impact experiment	Avg. propagation speed of primary wave front	3.6	[90]	[141]
ALON	Edge-on impact experiment	Wave propagation speed	10	[122, 123]	[34]
Steel	Kalthoff-Winkler experiment	Crack initiation time	3.4	[87]	[52]
Steel	Kalthoff-Winkler experiment	Crack propagation speed	14.2	[68, 101]	[17]
Ice	Crushing-brittle ice by a rotating cylinder	Mean force at 50 mm $s^{-1}$	74.3	[119]	[81]
Ice	Crushing-brittle ice by a rotating cylinder	Mean force at $130 \text{ mm s}^{-1}$	20.6	[119]	[81]
Ice	Crushing-brittle ice by a rotating cylinder	Mean force at $210 \text{ mm s}^{-1}$	25.1	[119]	[81]
Ice	Crushing-brittle ice by a rotating cylinder	Peak force at 50 mm s <sup>-1</sup>	66	[119]	[81]
Ice	Crushing-brittle ice by a rotating cylinder	Peak force at 130 mm s <sup>-1</sup>	11.7	[119]	[81]
Ice	Crushing-brittle ice by a rotating cylinder	Peak force at 210 mm s <sup>-1</sup>	29.1	[119]	[81]
Soda-lime glass	Pre-cracked glass (step tensile loading)	Max. crack propagation speed	6.3	[15]	[53]
Soda-lime glass	Pre-cracked plate (step tensile loading)	Max. crack propagation speed	26.8	[15]	[144]
Soda-lime glass	Pre-cracked plate (step tensile loading)	Max. crack propagation speed (16 281 nodes)	28.9	[15]	[52]
Soda-lime glass	Pre-cracked plate (step tensile loading)	Max. crack propagation speed (4141 nodes)	48.2	[15]	[52]
Soda-lime glass	Pre-cracked plate (step tensile loading)	Max. crack propagation speed (refined)	70.8	[15]	[52]
Concrete	Anchor Bolt Pullout (Configuration 1)	Peak loads	27.2	[128]	[83]
Concrete	Anchor Bolt Pullout (Configuration 2)	Peak loads	17.8	[128]	[83]
Concrete	Anchor Bolt Pullout (Configuration 3)	Peak loads	11.6	[128]	[83]

assess peridynamics simulations of fracture phenomena in solids. However, one should remember that visualization techniques involve models to approximate damage quantities, which should also be validated against experiments. For example, the crack growth velocity of the approximated crack surface was compared by Bußler et al. [17] with the one in the Kalthoff-Winkler experiment [68] in order to validate their model. The main objective of this section is to highlight the techniques that can be used for the comparison of peridynamics simulations with experiments.

#### 6.1 Visualization of Fragmentation

Material fragmentation is an example that can significantly benefit from visualization post-processing techniques. Fragmentation can be measured in terms of histograms of fragment size or fragment momentum and can thus be straightforwardly compared with experimental data [107, 129]. Littlewood et al. [79] developed an algorithm similar to the concept of fragment identification for classical finite element simulations [112] to extract fragments from PD simulations in terms of the nodes that are connected by unbroken bonds. Other attributes, like the mass or the momentum of each fragment, can also be provided. The algorithm was applied to bond-based peridynamics simulations of a brittle disc after impact by a spherical indenter inducing failure in the expanding ductile ring. For this example, Diehl et al. [29] extended a connectedcomponent labeling algorithm [104, 110] to identify fragments with respect to broken bonds obtained from a bond-based peridynamics simulation, as shown in Fig. 25a. In this figure, the nodes are colored with respect to the damage attribute (blue means no damage and red means damage based on broken bonds). Figure 25b shows the corresponding fragments associated with their labels, which are the identifiers of the fragments. In both algorithms, fragments are identified based on broken bonds and the assumption that damage arises at broken bonds. However, the algorithms have yet to be validated against experimental data. In our opinion, it would thus be instructive to compare the results of these methods with actual experiments to gain more insight about the peridynamics simulations, e.g., the influence of horizon values and variations in the initial positions on the fragment attributes.

#### 6.2 Visualization of Fracture Progression

Bußler et al. [17] developed a height ridge surface extraction approach to visualize fracture progression in peridynamics. The approach consists in approximating the crack surface and extracting other pertinent attributes, such as the fracture velocity or the crack angle, from the PD simulations. For instance, the crack angle and the crack growth velocity are provided in the Kalthoff-Winkler experiment [68]. Using only the "local" information available at the nodes, these quantities of interest are unfortunately not directly accessible from the simulations. Bußler et al. [17] demonstrated the efficiency of their algorithm on two



**Table 10**  $R^2$  correlation between the series of observables between experiment and simulation

Material	Mechanical test	Observable	$R^2$	Exp	Sim
Aluminum	Split-Hopkinson pressure bar	Strain vs time	0.99	[23]	[65]
Sandstone (Berea)	Wave dispersion	Dispersion curves at confining pressure of 10 MPa	0.84	[133]	[18]
Sandstone (Massilion)	Wave dispersion	Dispersion curves at confining pressure of 10 MPa	0.97	[133]	[18]
Sandstone (Berea)	Wave dispersion	Dispersion curves at confining pressure of 20 MPa	0.93	[133]	[18]
Sandstone (Massilion)	Wave dispersion	Dispersion curves at confining pressure of 20 MPa	1	[133]	[18]
Sandstone (Berea)	Wave dispersion	Dispersion curves at confining pressure of 40 MPa	0.95	[133]	[18]
Sandstone (Massilion)	Wave dispersion	Dispersion curves at confining pressure of 40 MPa	0.96	[133]	[18]
Columbia resin CR-39	Propagation of waves in a half-plane	Displacement vs position at 60 µs	0.74	[25]	[93]
Columbia resin CR-39	Propagation of waves in a half-plane	Displacement vs position at 92 µs	0.35	[25]	[93]
Columbia resin CR-39	Propagation of waves in a half-plane	Displacement vs position at 139 µs	0.15	[25]	[93]
Aluminum (6061-T6)	Taylor impact test	Norm diameter/length; strain vs stress	0.96	[4, 21]	[45]
Aluminum (6061-T6)	Ballistic impact test	Residual vel vs impact vel	0.99	[132]	[127]
Steel (4340 RC 43)	Split-Hopkinson pressure bar	Strain vs stress	0.97	[46]	[44]
Aluminum (D16AT)	Compact tension test	Force vs CMOD	1	[77, 131]	[135]
SAE 1020 steel	Compact tension test	Crack path position	0.97	[91]	[141]
Concrete	3-point bending	Load vs CMD	0.61	[63]	[51]
Concrete	3-point bending (D3)	Load vs CMOD	0.85	[19]	[ <mark>7</mark> ]
Concrete	3-point bending (D6)	Load vs CMOD	0.89	[19]	[ <mark>7</mark> ]
Concrete	3-point bending (D9)	Load vs CMOD	0.77	[19]	[ <mark>7</mark> ]
Concrete	3-point bending (D3 LPD-load)	Load vs LPD	0.87	[19]	[ <mark>7</mark> ]
Concrete	3-point bending (D6 LPD-load)	Load vs LPD	0.83	[19]	[ <mark>7</mark> ]
Concrete	3-point bending (D9 LPD-load)	Load vs LPD	0.51	[19]	[ <mark>7</mark> ]
Concrete	Anchor bolt pullout	Pullout load vs displacement	0.92	[128]	[83]
PMMA	Fast crack growth	Crack velocity vs time	0.72	[39]	[2]
PMMA	Tensile test	Poisson ratio vs time	0.65	[124]	[32]
FEM (Epoxy/Soda-lime glass)	3-point loading	Crack length vs time	0.99	[73]	[24]

Abbreviations: crack mouth displacement (CMD), crack mouth opening displacement (CMOD), and load point displacement (LPD)

examples, namely, the thin disk impacted by a spherical indenter and the Stanford Bunny. Moreover, they validated the extracted fracture growth velocity with the one obtained in the Kalthoff-Winkler experiment (see Table 12). The fracture growth velocity was predicted as 1140 m s<sup>-1</sup>, that is a 14% relative error when compared to the value obtained in the experiment. A similar study using the smoothed-particle hydrodynamics method (SPH) [101] provided a velocity of 1200 m s<sup>-1</sup> or a 20% relative error. Nevertheless, it would be important to further analyze the influence of the initial node positions and the axis-alignment of the crack surfaces on the predicted velocity.

#### 6.3 Physically Based Modeling and Rendering

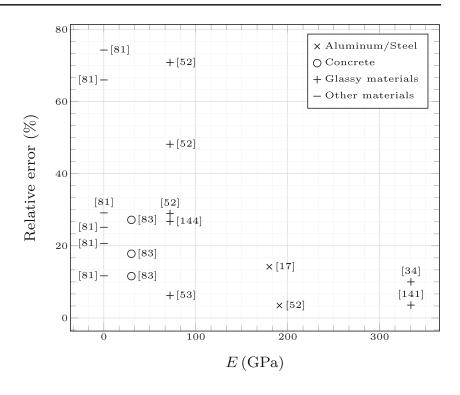
Another interesting application of peridynamics could be for physically based modeling and rendering of visual effects [78, 99]. Peridynamics, thanks to the comparative simplicity of the models, could indeed provide a good balance between artistic rendering and accuracy in describing physical behaviors. For example, Levine et al. [78] used bond-based PD for the animation of brittle fracture. Levine et al. [78] animated the impact of a projectile through a glass plate and the fracturing of the Welsh dragon/vase on the floor. Levine et al. [78] reported that as in most physics-based animation methods, tuning parameters can be a tedious task.

Chen et al. [22] used state-based PD for the animation of fractures in elastoplastic solids. Chen et al. [22] visualized the isotropic brittle, anisotropic brittle, isotropic ductile, and anisotropic ductile fracture behavior of a sphere travelling through a wall. Next, Chen et al. [22] visualized the complex crack pattern when shooting a bullet through jello, the fragments obtained in the case of the Stanford bunny<sup>3</sup> falling to the ground, and the crack pattern in a thin sheet when pulled apart. Chen et al. [22] concluded that the horizon needed sometimes to be fine-tuned in order to get well-synchronized results.



<sup>&</sup>lt;sup>3</sup>http://graphics.stanford.edu/data/3Dscanrep/

**Fig. 23** Relative error versus the Young modulus *E* of the material used in the experiments. Note that some of the values were post-processed by extracting the data from plots provided in the publications



#### 7 Concluding Remarks and Perspectives

Applications for validation of bond-based PD and statebased PD were reviewed and summarized in Tables 1 and 3. Overall, we identified 22 applications for bondbased PD and 9 applications for state-based PD. In the case of applications dealing with initiation and propagation of cracks, we chose to classify the contributions with respect to the type of materials, namely composites, aluminum/steel, glassy materials, concrete, and other materials. The Kalthoff-Winkler experiment was used to assess the crack initiation time, the crack propagation speed, and the crack angle. We thus believe that the Kalthoff-Winkler experiment could be a valuable benchmark for the

Fig. 24 Coefficient of determination  $R^2$  versus the Young modulus E of the material used in the experiments. Note that some values were post-processed by extracting the data from plots provided in the publications

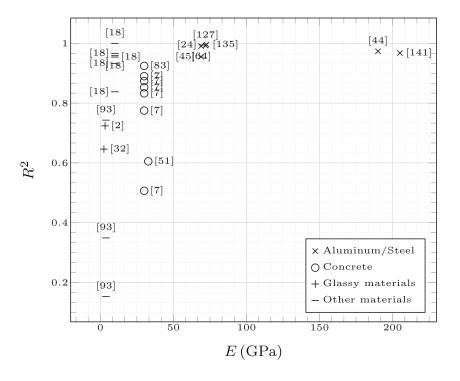




**Table 11** Overview of applications of bond-based (B) and state-based (S) peridynamics simulations using visualization algorithms to assess fracture in solids

Application	В	S	Reference
Animation of brittle fracture	<b>√</b>		[78]
Fracture animation in elastoplastic solids		$\checkmark$	[22]
Fracture progression	$\checkmark$	$\checkmark$	[17]
Extraction of fragments	$\checkmark$		[29, 79]

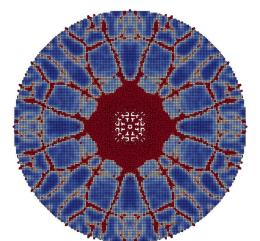
validation of PD models, since it provides three different types of measurement at once. In other words, it is challenging to simultaneously predict the three observables.

We also indicated, to some extent, whether the comparative studies between simulations and experiments were quantitative or qualitative. In most cases, we were able to compute either the relative error, for scalar observables, or the coefficient of determination  $R^2$ , for series of observables, to assess the predictability of the PD models.

The major results of this investigation are collected in Tables 9 and 10 and plotted in Figs. 23 and 24. We note that the best correlations were obtained for edge-on impact (EOI) experiment experiments involving aluminum and steel materials.

It is commonly accepted that the size of the PD horizon should be set to three or four times the mesh size. Nevertheless, some authors have studied the influence of the horizon  $\delta$  and mesh size on the predictions. For example, Zhang [141] investigated the influence of the horizon on the position of the crack path: the values of  $R^2$  were estimated at 0.97 and 0.99 for  $\delta = 1.2$  mm and  $\delta = 0.6$  mm, respectively. Gu et al. [52] looked at the effect of

Fig. 25 Illustration of fragmentation of a thin disk following impact by a spherical indenter using an extended connected-component labeling algorithm [29]



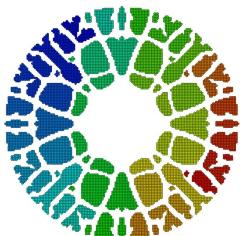
(a) Scattered nodes after impact of a spherical indenter. Color indicates damage (Blue means no damage while red means all bonds are broken).

**Table 12** Comparison of the fracture growth velocity obtained in the Kalthoff-Winkler experiment [68] with that predicted by peridynamics (PD) [17] and smoothed-particle hydrodynamics (SPH) [101]

Setting	Fracture growth velocity m s <sup>-1</sup>
Experiment	1000
SPH	1200
PD	Mean 1142, median 1144

mesh size on the maximal speed of crack propagation: the values obtained in the simulations were  $2341 \text{ m s}^{-1}$  and  $2037 \text{ m s}^{-1}$  for uniformly distributed 4141 nodes and 16281 nodes, respectively. Unsurprisingly, simulations are clearly influenced by the choice of the discretization and the value of the horizon.

Applications of computer graphics have usually two objectives: (1) to gain more realistic visual effects using physics-based modeling and rendering; (2) to reconstruct from the solutions large-scale quantities or features, such as number of fragments and shape of the crack surfaces. In all reconstruction approaches, the approximation of damage in PD is based on the notion that damage arises at broken bonds. Unfortunately, validation of these models against experimental data is still lacking at this time. There is maybe one exception in which extraction of crack surfaces in the Kalthoff-Winkler experiment was used with partial success to measure the fracture growth velocity. We believe that advanced visualization techniques could be useful to gain more insight on the effect of initial positions of the discrete PD nodes on quantities of interest, such as the fragment size or alignment of crack surfaces. They could also help investigate optimal ratios between the horizon and mesh size.



(b) Extracted fragments with associated la-



Following this comprehensive study, our opinion is that there remain many issues and challenges in order to fully assess peridynamics models with respect to experiments:

- Poundary conditions: One of the major challenges pertains to the treatment of boundary conditions when dealing with non-local models [37, 50, 85, 86]. This is an issue that one also finds in molecular dynamics simulations or in smooth particles hydrodynamics. To overcome this issue, several approaches for coupling PD with the finite element method (FEM) or classical continuum mechanics (CCM), e.g., force-based blending [108, 109], Arlequin approach [55], or discrete coupling [47, 72, 82, 84, 111, 138, 139] have been developed. One could use a coupling approach in order to enforce boundary conditions, that is, by using CCM or FEM along the boundaries and PD in the region of interest where cracks and fractures arise.
- Discretization parameters: For the discrete case, the choice of the nodal spacing and the horizon influences the various convergence scenarios [38, 126]. One issue is defining the proper ratio between the horizon and mesh size as numerical results are certainly sensitive [30] to these two parameters. One approach is to adjust the horizon, so that the peridynamic results produce the same dispersion curves as those measured for a specific material [115]. Another approach is to determine the horizon by Griffith's brittle failure criterion, based on critical failure stress which can be found experimentally [32].
- Computational costs: The computational costs for non-local models, like PD, are significant. Some cited references were not able to simulate the full size of the experimental geometry, due to computational limitations. Several massive parallel peridynamics implementations are available: Peridigm [80, 97] and PDLammps [98] based on the Message Passing Interface (MPI), peridynamicHPX [31] based on the C++ standard library for parallelism and concurrency (HPX) [56], acceleration card codes based on OpenCL [92] or on CUDA [27, 33].
- Calibration versus validation: Simulations are usually compared to experimental data for *calibration/fitting* or *validation*. In the first case, the material parameters are calibrated, such that they fit observable quantities in a given experiment, e.g., reproduce the same dispersion curve or the crack growth velocity. In the second case, the calibrated parameters are used for validation against other experimental scenarios, e.g., different loading values or different positions of the initial crack. In the majority of the cited references, the material parameters

were calibrated against one experiment and only a few addressed validation.

#### References

- Abanto-Bueno J, Lambros J (2006) An experimental study of mixed mode crack initiation and growth in functionally graded materials. Exp Mech 46(2):179–196
- Agwai A, Guven I, Madenci E (2011) Predicting crack propagation with peridynamics: a comparative study. Int J Fract 171(1):65
- Amani J, Oterkus E, Areias P, Zi G, Nguyen-Thoi T, Rabczuk T (2016) A non-ordinary state-based peridynamics formulation for thermoplastic fracture. Int J Impact Eng 87(SI):83–94
- 4. Anderson CE, Nicholls AE, Chocron IS, Ryckman RA (2006) Taylor anvil impact. AIP Conf Proc 845(1):1367–1370
- ASTM International (2000) ASTM E647-00 standard test method for measurement of fatigue crack growth rates
- Awerbuch J, Madhukar MS (1985) Notched strength of composite laminates: Predictions and experiments—a review. J Reinf Plast Compos 4(1):3–159
- Aziz A (2014) Simulation of fracture of concrete using micropolar peridynamics. Ph.D. thesis, University of New Mexico
- Ball A, McKenzie H (1994) On the low velocity impact behaviour of glass plates. J Phys IV 4(C8):C8–783
- 9. Boardman B (1990) Fatigue resistance of steels, vol 1
- Bobaru F, Foster JT, Geubelle PH, Silling SA (2016) Handbook of peridynamic modeling. CRC Press, Boca Raton
- Bobaru F, Yang M, Alves LF, Silling SA, Askari E, Xu J (2009) Convergence, adaptive refinement, and scaling in 1d peridynamics. Int J Numer Methods Eng 77(6):852–877
- Bogert P, Satyanarayana A, Chunchu P (2006) Comparison of damage path predictions for composite laminates by explicit and standard finite element analysis tools. In: Collection of technical papers - AIAA/ASME/ASCE/AHS/ASC structures, structural dynamics and materials conference, vol 3
- Bouchbinder E, Hentschel HGE, Procaccia I (2003) Dynamical instabilities of quasistatic crack propagation under thermal stress. Phys Rev E 68:036,601
- Boudet J, Ciliberto S, Steinberg V (1996) Dynamics of crack propagation in brittle materials. J Phys II 6(10):1493–1516
- Bowden F, Brunton J, Field J, Heyes A (1967) Controlled fracture of brittle solids and interruption of electrical current. Nature 216(5110):38–42
- Bowden FP, Field JE (1964) The brittle fracture of solids by liquid impact, by solid impact, and by shock. Proceedings of the Royal Society of London A: Mathematical, Physical and Engineering Sciences 282(1390):331–352
- Bußler M, Diehl P, Pflüger D, Frey S, Sadlo F, Ertl T, Schweitzer MA (2017) Visualization of fracture progression in peridynamics. Comput Graph 67:45–57
- Butt SN, Timothy JJ, Meschke G (2017) Wave dispersion and propagation in state-based peridynamics. Comput Mech 60(5):725–738
- Chapman S (2011) Clariffication of the notched beam level in testing procedures of ACI 446 committee report 5. Master's thesis, University of New Mexico
- Chaudhri MM, Walley SM (1978) Damage to glass surfaces by the impact of small glass and steel spheres. Philos Mag A 37(2):153–165



- Chen W, Song B, Frew DJ (2002) 108 split Hopkinson bar testing of an aluminum with pulse shaping. The Proceedings of the JSME Materials and Processing Conference (M&P) 10.1:58–61
- Chen W, Zhu F, Zhao J, Li S, Wang G (2017) Peridynamics-based fracture animation for elastoplastic solids. Comput Graph Forum 37(1):112–124
- 23. Chen WW, Song B (2011) Mechanical engineering series. In: Split Hopkinson (Kolsky) bar design, testing and applications, vol 1. Springer, US, p 388
- Cheng Z, Zhang G, Wang Y, Bobaru F (2015) A peridynamic model for dynamic fracture in functionally graded materials. Compos Struct 133:529–546
- Dally J, Thau S (1967) Observations of stress wave propagation in a half-plane with boundary loading. Int J Solids Struct 3(3):293–308
- Devore JL (2012) Probability and statistics for engineering and the sciences, 2nd edn. Springer, New York
- Diehl P (2012) Implementierung eines Peridynamik-Verfahrens auf GPU. Diplomarbeit, Institute of Parallel and Distributed Systems, University of Stuttgart
- Diehl P (2017) Modeling and simulation of cracks and fractures with peridynamics in brittle materials. Phd. thesis, Institut für Numerische Simulation, Universit ät Bonn
- Diehl P, Bußler M, Pflüger D, Frey S, Ertl T, Sadlo F, Schweitzer MA (2017) Extraction of fragments and waves after impact damage in particle-based simulations. In: Meshfree methods for partial differential equations VIII. Springer International Publishing, pp 17–34
- Diehl P, Franzelin F, Pflüger D, Ganzenmüller GC (2016) Bond-based peridynamics: a quantitative study of mode i crack opening. Int J Fract 201(2):157–170
- Diehl P, Jha PK, Kaiser H, Lipton R, Lévesque M (2018)
   Implementation of peridynamics utilizing hpx-the c++ standard library for parallelism and concurrency. arXiv:1806.06917
- 32. Diehl P, Lipton R, Schweitzer MA (2016) Numerical verification of a bond-based softening peridynamic model for small displacements: Deducing material parameters from classical linear theory. Tech. rep., Institut für Numerische Simulation
- Diehl P, Schweitzer MA (2015) Efficient neighbor search for particle methods on gpus. In: Meshfree methods for partial differential equations VII. Springer, pp 81–95
- Diehl P, Schweitzer MA (2015) Simulation of wave propagation and impact damage in brittle materials using peridynamics. In: Recent trends in computational engineering-CE2014. Springer, pp 251–265
- Diehl P, Tabiai I, Baumann FW, Therriault D, Lévesque M (2018) Long term availability of raw experimental data in experimental fracture mechanics. Eng Fract Mech 197:21–26
- Döll W (1975) Investigations of the crack branching energy. Int J Fract 11(1):184–186
- Du Q (2016) Nonlocal calculus of variations and well-posedness of peridynamics. Handbook of Peridynamic Modeling 63–85
- Du Q, Tian X (2015) Robust discretization of nonlocal models related to peridynamics. In: Meshfree methods for partial differential equations VII. Springer, pp 97–113
- Eran S, Fineberg J (1999) Confirming the continuum theory of dynamic brittle fracture for fast cracks. Nature 397(6717):333
- Field J (1988) Investigation of the impact performance of various glass and ceramic systems. Tech. rep., Cambridge University (United Kingdom) Cavebdish Laboratory
- Fineberg J, Gross SP, Marder M, Swinney HL (1992) Instability in the propagation of fast cracks. Phys Rev B 45:5146–5154
- Fineberg J, Marder M (1999) Instability in dynamic fracture. Phys Rep 313(1):1–108

- Foster JT (2009) Dynamic crack initiation toughness: Experiments and peridynamic modeling. Sandia Report SAN D2009-7217, Sandia National Laboratories
- 44. Foster JT, Silling SA, Chen WW (2009) State based peridynamic modeling of dynamic fracture. In: Annual conference and exposition on experimental and applied mechanics 2009 society for experimental mechanics - SEM, vol 4, pp 2312–2317
- 45. Foster JT, Silling SA, Chen WW (2010) Viscoplasticity using peridynamics. Int J Numer Methods Eng 81(10):1242–1258
- Frew DJ, Forrestal MJ, Chen W (2005) Pulse shaping techniques for testing elastic-plastic materials with a split Hopkinson pressure bar. Exp Mech 45(2):186
- Galvanetto U, Mudric T, Shojaei A, Zaccariotto M (2016) An effective way to couple fem meshes and peridynamics grids for the solution of static equilibrium problems. Mech Res Commun 76:41–47
- 48. Gerstle W, Sakhavand N, Chapman S (2010) Peridynamic and continuum models of reinforced concrete lap splice compared. fracture mechanics of concrete and concrete structures-recent advances in fracture mechanics of concrete
- Gözen I, Dommersnes P, Czolkos I, Jesorka A, Lobovkina T, Orwar O (2010) Fractal avalanche ruptures in biological membranes. Nat Mater 9(11):908
- 50. Gu X, Madenci E, Zhang Q (2018) Revisit of non-ordinary state-based peridynamics. Eng Fract Mech 190:31–52
- Gu X, Wu Q (2016) The application of nonordinary, statebased peridynamic theory on the damage process of the rock-like materials. Math Probl Eng 2016, 9 pp
- Gu X, Zhang Q, Xia X (2017) Voronoi-based peridynamics and cracking analysis with adaptive refinement. Int J Numer Methods Eng 112(13):2087–2109
- Ha YD, Bobaru F (2010) Studies of dynamic crack propagation and crack branching with peridynamics. Int J Fract 162(1):229– 244
- Haeri H, Shahriar K, Marji MF, Moarefvand P (2014) Experimental and numerical study of crack propagation and coalescence in pre-cracked rock-like disks. Int J Rock Mech Min Sci 67:20–28
- Han F, Lubineau G (2012) Coupling of nonlocal and local continuum models by the arlequin approach. Int J Numer Methods Eng 89(6):671–685
- Heller T, Diehl P, Byerly Z, Biddiscombe J, Kaiser H (2017) Hpx-an open source c++ standard library for parallelism and concurrency
- 57. Hopkinson B (1914) A method of measuring the pressure produced in the detonation of high explosives or by the impact of bullets. Philosophical Transactions of the Royal Society of London Series A, Containing Papers of a Mathematical or Physical Character 213(497–508):437–456
- Hu W, Ha YD, Bobaru F (2011) Modeling dynamic fracture and damage in a fiber-reinforced composite lamina with peridynamics. Int J Multiscale Comput Eng 9(6)
- Hu W, Wang Y, Yu J, Yen CF, Bobaru F (2013) Impact damage on a thin glass plate with a thin polycarbonate backing. Int J Impact Eng 62:152–165
- 60. Humphrey W, Dalke A, Schulten K (1996) VMD visual molecular dynamics. J Mol Graph 14:33–38
- 61. Ihmsen M, Orthmann J, Solenthaler B, Kolb A, Teschner M (2014) SPH fluids in computer graphics. In: Lefebvre S, Spagnuolo M (eds) Eurographics 2014 state of the art reports. The Eurographics association
- 62. International Organization for Standardization (2003) Corrosion of metals and alloys - stress corrosion testing - part 6: Preparation and use of pre-cracked specimens for tests under constant load or constant displacement



- Jenq YS, Shah SP (1988) Mixed-mode fracture of concrete. Int J Fract 38(2):123–142
- Jia T (2012) Development and applications of new peridynamic models. Ph.D. thesis, Michigan State University
- Jose S, Kumar RR, Jana M, Rao GV (2001) Intralaminar fracture toughness of a cross-ply laminate and its constituent sub-laminates. Compos Sci Technol 61(8):1115–1122
- Kalthoff JF (1988) Shadow optical analysis of dynamic shear fracture. Opt Eng 27(10):271,035
- Kalthoff JF (2000) Modes of dynamic shear failure in solids. Int J Fract 101(1):1–31
- Kalthoff JF, Winkler S (1988) Failure mode transition at high rates of shear loading. Impact Loading and Dynamic Behavior of Materials 1:185–195
- Kawai M, Morishita M, Satoh H, Tomura S, Kemmochi K (1997) Effects of end-tab shape on strain field of unidirectional carbon/epoxy composite specimens subjected to off-axis tension. Compos A: Appl Sci Manuf 28(3):267–275
- Kilic B, Agwai A, Madenci E (2009) Peridynamic theory for progressive damage prediction in center-cracked composite laminates. Compos Struct 90(2):141–151
- Kilic B, Madenci E (2009) Prediction of crack paths in a quenched glass plate by using peridynamic theory. Int J Fract 156(2):165–177
- 72. Kilic B, Madenci E (2010) Coupling of peridynamic theory and the finite element method. J Mech Mater Struct 5(5):707–733
- Kirugulige M, Tippur HV (2008) Mixed-mode dynamic crack growth in a functionally graded particulate composite: experimental measurements and finite element simulations. J Appl Mech 75(5):051,102
- Kirugulige MS, Tippur HV (2006) Mixed-mode dynamic crack growth in functionally graded glass-filled epoxy. Exp Mech 46(2):269–281
- Kitey R, Tippur HV (2008) Dynamic crack growth past a stiff inclusion: optical investigation of inclusion eccentricity and inclusion-matrix adhesion strength. Exp Mech 48(1):37–53
- Kolsky H (1949) An investigation of the mechanical properties of materials at very high rates of loading. Proc Phys Soc Sect B 62(11):676
- 77. Kumar S, Singh I, Mishra B (2014) A coupled finite element and element-free Galerkin approach for the simulation of stable crack growth in ductile materials. Theor Appl Fract Mech 70(Supplement C):49–58
- Levine JA, Bargteil AW, Corsi C, Tessendorf J, Geist R (2014) A peridynamic perspective on spring-mass fracture. In: Proceedings of the ACM SIGGRAPH/Eurographics symposium on computer animation, SCA '14, pp 47–55. Eurographics association
- Littlewood D, Silling S, Demmie P (2016) Identification of fragments in a meshfree peridynamic simulation. In: ASME 2016 international mechanical engineering congress and exposition, pp V009T12A071–V009T12A071. American society of mechanical engineers
- Littlewood DJ (2015) Roadmap for Peridynamic Software Implementation. Tech Rep 2015-9013, Sandia National Laboratories
- Liu M, Wang Q, Lu W (2017) Peridynamic simulation of brittleice crushed by a vertical structure. Int J Naval Architecture Ocean Eng 9(2):209–218
- Liu W, Hong JW (2012) A coupling approach of discretized peridynamics with finite element method. Comput Methods Appl Mech Eng 245:163–175
- 83. Lu J, Zhang Y, Muhammad H, Chen Z (2018) Peridynamic model for the numerical simulation of anchor bolt pullout in concrete. Math Probl Eng 2018:1–10

- 84. Madenci E, Barut A, Dorduncu M, Phan ND (2018) Coupling of peridynamics with finite elements without an overlap zone. In: 2018 AIAA/ASCE/AHS/ASC structures, structural dynamics, and materials conference, p 1462
- Madenci E, Dorduncu M, Barut A, Phan N (2018) A state-based peridynamic analysis in a finite element framework. Eng Fract Mech 195:104–128
- 86. Madenci E, Dorduncu M, Barut A, Phan N (2018) Weak form of peridynamics for nonlocal essential and natural boundary conditions. Comput Methods Appl Mech Eng 337:598–631
- 87. Madenci E, Oterkus E (2014) Peridynamic theory and its applications, vol 17. Springer, New York
- 88. Madenci E, Oterkus E (2014) Peridynamic theory and its applications, chap 2 peridynamic theory, vol 17. Springer, Berlin, pp 19–43
- 89. Mahanty D, Maiti S (1990) Experimental and finite element studies on mode I and mixed mode (I and II) stable crack growth—I. Exp Eng Fracture Mech 37(6):1237–1250
- McCauley J, Strassburger E, Patel P, Paliwal B, Ramesh K
   (2013) Experimental observations on dynamic response of selected transparent armor materials. Exp Mech 53(1):3–29
- Miranda A, Meggiolaro M, Castro J, Martha L, Bittencourt T (2003) Fatigue life and crack path predictions in generic 2d structural components. Eng Fract Mech 70(10):1259–1279
- Mossaiby F, Shojaei A, Zaccariotto M, Galvanetto U (2017)
   Opencl implementation of a high performance 3d peridynamic model on graphics accelerators. Comput Math Appl 74(8): 1856–1870
- Nishawala VV, Ostoja-Starzewski M, Leamy MJ, Demmie PN (2016) Simulation of elastic wave propagation using cellular automata and peridynamics, and comparison with experiments. Wave Motion 60:73–83
- Ocaña I, Molina-Aldareguia J, Gonzalez D, Elizalde M, Sánchez J, Martinez-Esnaola J, Sevillano JG, Scherban T, Pantuso D, Sun B (2006) Fracture characterization in patterned thin films by cross-sectional nanoindentation. Acta Mater 54(13):3453–3462
- 95. Oterkus E, Agwai A, Guven I, Madenci E (2009) Peridynamic theory for simulation of failure mechanisms in electronic packages. In: ASME 2009 InterPACK Conference collocated with the ASME 2009 summer heat transfer conference and the ASME 2009 3rd international conference on energy sustainability, pp 63–68. American Society of Mechanical Engineers
- 96. Oterkus E, Barut A, Madenci E (2010) Damage growth prediction from loaded composite fastener holes by using peridynamic theory. In: Collection of technical papers -AIAA/ASME/ASCE/AHS/ASC structures, structural dynamics and materials conference, pp 1–14
- Parks M, Littlewood D, Mitchell J, Silling S (2012) Peridigm users' guide. Tech Rep SAND2012-7800, Sandia National Laboratories
- Parks ML, Lehoucq RB, Plimpton SJ, Silling SA (2008) Implementing peridynamics within a molecular dynamics code. Comput Phys Commun 179(11):777–783
- Pharr M, Jakob W, Humphreys G (2016) Physically based rendering: from theory to implementation, 3rd edn. Morgan Kaufmann, San Mateo
- 100. Ramulu M, Kobayashi AS (1985) Mechanics of crack curving and branching — a dynamic fracture analysis. Int J Fract 27(3):187–201
- 101. Raymond S, Lemiale V, Ibrahim R, Lau R (2014) A meshfree study of the Kalthoff–Winkler experiment in 3D at room and low temperatures under dynamic loading using viscoplastic modelling. Engineering Analysis with Boundary Elements 42:20–25



- Ronsin O, Perrin B (1997) Multi-fracture propagation in a directional crack growth experiment. EPL (Europhysics Letters) 38(6):435
- Ronsin O, Perrin B (1998) Dynamics of quasistatic directional crack growth. Phys Rev E 58:7878–7886
- Rosenfeld A, Pfaltz JL (1966) Sequential operations in digital picture processing. J ACM 13(4):471–494
- 105. Sanchez J, El-Mansy S, Sun B, Scherban T, Fang N, Pantuso D, Ford W, Elizalde M, Martinez-Esnaola J, Martin-Meizoso A et al (1999) Cross-sectional nanoindentation: a new technique for thin film interfacial adhesion characterization. Acta Materialia 47(17):4405–4413
- 106. Satyanarayana A, Bogert P, Chunchu P (2017) The effect of delamination on damage path and failure load prediction for notched composite laminates. In: 48th AIAA/ASME/ ASCE/AHS/ASC structures, structural dynamics, and materials conference, p 1993
- Schram S, Meyer H (2005) Simulating the formation and evolution of behind armor debris fields. ARL-RP 109, US Army Research Laboratory
- Seleson P, Beneddine S, Prudhomme S (2013) A force-based coupling scheme for peridynamics and classical elasticity. Comput Mater Sci 66:34

  –49
- Seleson P, Ha YD, Beneddine S (2015) Concurrent coupling of bond-based peridynamics and the navier equation of classical elasticity by blending. Int J Multiscale Comput Eng 13(2)
- 110. Shapiro LG (1996) Connected component labeling and adjacency graph construction. In: Kong TY, Rosenfeld A (eds) Topological algorithms for digital image processing, machine intelligence and pattern recognition, vol 19. North-Holland, pp 1–30
- 111. Shojaei A, Mudric T, Zaccariotto M, Galvanetto U (2016) A coupled meshless finite point/peridynamic method for 2d dynamic fracture analysis. Int J Mech Sci 119:419–431
- 112. SIERRA Solid Mechanics Team (2016) Sierra/SolidMechanics 4.40 User's Guide. Tech. Rep. SAND2016-2707 O, Sandia National Laboratories, Albuquerque, NM and Livermore, CA
- Silling SA (2000) Reformulation of elasticity theory for discontinuities and long-range forces. J Mech Phys Solids 48(1):175–209
- 114. Silling SA (2002) Peridynamic modeling of the Kalthoff-Winkler experiment submission for the 2001 Sandia prize in computational science
- Silling SA (2011) A coarsening method for linear peridynamics.
   Int J Multiscale Comput Eng 9(6):609–622
- Silling SA (2016) Why peridynamics? Handbook of Peridynamic Modeling: 1
- Silling SA, Askari E (2005) A meshfree method based on the peridynamic model of solid mechanics. Comput Struct 83(17):1526–1535
- 118. Silling SA, Epton M, Weckner O, Xu J, Askari E (2007) Peridynamic states and constitutive modeling. J Elast 88(2):151– 184
- Sodhi DS, Morris CE (1986) Characteristic frequency of force variations in continuous crushing of sheet ice against rigid cylindrical structures. Cold Reg Sci Technol 12(1):1–12
- Starikov R, Schön J (2002) Local fatigue behaviour of cfrp bolted joints. Compos Sci Technol 62(2):243–253
- Strassburger E (2004) Visualization of impact damage in ceramics using the edge-on impact technique. Int J Appl Ceram Technol 1:235–242
- 122. Strassburger E, Patel P, McCauley JW, Tempelton DW (2005) Visualization of wave propagation and impact damage in a polycrystalline transparent ceramic AlON. In: 22nd international symposium on ballistics, vol 2, pp 769–776

- 123. Strassburger E, Patel P, McCauley JW, Templeton DW (2006) High-speed photographic study of wave propagation and iimpact damage in fused silcia and alon using the edge-on impact (EOI) method. AIP Conf Proc 845:892–895
- 124. Tabiai I (2017) PMMA tensile test until failure, loaded in force.
- 125. Taylor M, Gözen I, Patel S, Jesorka A, Bertoldi K (2016) Peridynamic modeling of ruptures in biomembranes. PloS one 11(11):e0165, 947
- 126. Tian X, Du Q (2014) Asymptotically compatible schemes and applications to robust discretization of nonlocal models. SIAM J Numer Anal 52(4):1641–1665
- Tupek M, Rimoli J, Radovitzky R (2013) An approach for incorporating classical continuum damage models in state-based peridynamics. Comput Methods Appl Mech Eng 263:20–26
- 128. Vervuurt A, Van Mier JG, Schlangen E (1994) Analyses of anchor pull-out in concrete. Mater Struct 27(5):251–259
- 129. Vogler TJ, Thornhill TF, Reinhart WD, Chhabildas LC, Grady DE, Wilson LT, Hurricane OA, Sunwoo A (2003) Fragmentation of materials in expanding tube experiments. Int J Impact Eng 29(1–10):735–746
- 130. Wang Y (2015) Peridynamic studies of interactions between stress waves and propagating cracks in brittle solids. Ph.D. thesis, University of Nebraska
- Weng T, Sun C (2000) A study of fracture criteria for ductile materials. Eng Fail Anal 7(2):101–125
- 132. Wetzel JJ (2009) The impulse response of extruded corrugated core aluminum sandwich structures. Master's thesis, University of Virginia
- 133. Winkler KW (1983) Frequency dependent ultrasonic properties of high-porosity sandstones. J Geophys Res Solid Earth 88(B11):9493–9499
- 134. Wu E (1967) Application of fracture mechanics to anisotropic plates. Trans ASME J Appl Mech 34(4):967–974
- Yolum U, Taştan A, Güler MA (2016) A peridynamic model for ductile fracture of moderately thick plates. Procedia Structural Integrity 2:3713–3720
- Yuse A, Sano M (1993) Transition between crack patterns in quenched glass plates. Nature 362(6418):329–331
- Yuse A, Sano M (1997) Instabilities of quasi-static crack patterns in quenched glass plates. Physica D: Nonlinear Phenomena 108(4):365–378
- Zaccariotto M, Mudric T, Tomasi D, Shojaei A, Galvanetto U (2018) Coupling of fem meshes with peridynamic grids. Comput Methods Appl Mech Eng 330:471–497
- Zaccariotto M, Tomasi D, Galvanetto U (2017) An enhanced coupling of pd grids to fe meshes. Mech Res Commun 84:125– 135
- 140. Zhang F, Wu J, Shen X (2011) SPH-based fluid simulation: a survey. In: Proceedings - 2011 international conference on virtual reality and visualization, ICVRV 2011, pp 164–171
- 141. Zhang G (2017) Peridynamic models for fatigue and fracture in isotropic and in polycrystalline materials. Ph.D. thesis, University of Nebraska
- 142. Zhang G, Bobaru F (2016) Modeling The Evolution of Fatigue Failure with Peridynamics. In: Ro J Techn Sci Appl Mechanics, vol 1, pp 22–40
- 143. Zhang JJ, Bentley LR (1999) Change of bulk and shear moduli of dry sandstone with effective pressure and temperature. CREWES Research Report 11:01–16
- 144. Zhou X, Wang Y, Qian Q (2016) Numerical simulation of crack curving and branching in brittle materials under dynamic loads using the extended non-ordinary state-based peridynamics. Eur J Mech A Solids 60:277–299

